

Lawrence Berkeley National Laboratory

Lawrence Berkeley National Laboratory

Title

Surface chemistry controls crystallinity of ZnS nanoparticles

Permalink

<https://escholarship.org/uc/item/8123j9dc>

Authors

Gilbert, Benjamin

Huang, Feng

Lin, Zhang

et al.

Publication Date

2005-12-20

Peer reviewed

Surface chemistry controls crystallinity of ZnS nanoparticles

*Benjamin Gilbert¹, Feng Huang², Zhang Lin², Carmen Goodell³, Hengzhong Zhang³ and Jillian F.
Banfield³*

1. Earth Sciences Division, Lawrence Berkeley National Lab., Berkeley, CA 94720

2. Fujian Institute of Research on the Structure of Matter, Chinese Academy of Sciences, Fuzhou,
Fujian, 350002, People's Republic of China

3. Department of Earth and Planetary Sciences, University of California – Berkeley, Berkeley, CA
94720

bgilbert@lbl.gov, jill@eps.berkeley.edu

RECEIVED DATE (to be automatically inserted)

TITLE RUNNING HEAD: ZnS Nanoparticle Crystallinity

ABSTRACT Combined small-angle and high energy wide-angle x-ray scattering measurements of nanoparticle size and structure permit interior strain and disorder to be directly observed in the real-space pair distribution function (PDF). PDF analysis showed that samples of ZnS nanoparticle with similar mean diameters (3.2 – 3.6 nm) but synthesized and treated differently possess a dramatic range

of interior disorder. We used Fourier transform infra-red spectroscopy to detect the surface species and the nature of surface chemical interactions. Our results suggest that there is a direct correlation between the strength of surface-ligand interactions and interior crystallinity.

KEYWORDS nanoparticle structure; ZnS; pair distribution function; small-angle x-ray scattering

BRIEFS *A one-sentence synopsis for inclusion in the Table of Contents – is this needed?*

INTRODUCTION

Inorganic nanoparticles are a distinct class of matter because their properties can be substantially modified relative to the bulk material. In some systems, typified by the cadmium chalcogenides, quantum confinement (a pure size effect) leads to size-tunable electronic behavior (1)(2). For other substances, including many metal oxides, nanoparticles are found to adopt a structural phase that is metastable in the bulk (3)(4). Thus, the properties of nanoparticles are a function of both size, and size-induced structural effects.

Due to the lack of established experimental methods to define the structural state of nanoparticles, it is frequently assumed that they are defect-free and internally unstrained (5)(6). More recent theoretical (7)(8) and experimental results (9)(10) indicate that these assumptions may be invalid. Disorder and defects can contribute significantly to the material and electronic properties of bulk crystals (11)**Error! Reference source not found.** If present in nanoparticles, disorder and defects will significantly modify materials properties, and hence there is a strong motivation for pursuing experimental approaches that are sensitive to the details of nanoparticle structure. EXAFS analyses of nanoparticles often showed the presence of excess static disorder in nanoparticles (12)(14)(15). Debye Function Analysis has been applied to estimate stacking fault frequencies (16)(17) and a pair distribution function (PDF) based analysis has been used to quantify internal strain in nanoparticles (18). However, there is no general picture of the incidence and nature of crystalline imperfections in nanoparticles.

While a great deal of attention has been given to controlling nanoparticle size and size distribution, it is less clear whether nanoparticle crystallinity is determined by temperature, the kinetics of the growth pathway, or by specific surface ligand interactions. There are strong experimental indications that nanoparticles are dynamic systems at room temperature. For example, complete cation exchange can occur extremely rapidly within CdSe nanoparticles in Ag solution (19), and solvent effects (9) or aggregation (20) can cause profound changes in nanoparticle structure. The implications of these findings are that surface interactions are the dominant factor in nanoparticle crystallinity, and that the

thermodynamic stable structure of individual nanoparticles is kinetically accessible at room temperature.

Many experimental and theoretical studies have considered the interactions between nanoparticles and different types of surface ligands. Such work revealed that surface ligands can determine important properties, including optical absorption threshold position (15)(21) and photoluminescence efficiency (22). No correlation has been made, however, between the type of surface ligand and the detailed nanoparticle structure. Here we show that different types of interactions at the surface of ZnS nanoparticles can result in a very large range of internal crystallinity for nanoparticles of the same size.

EXPERIMENTAL SECTION.

ZnS nanoparticles approximately 3 nm in diameter were synthesized by three methods and with subsequent treatments we produced nanoparticles with four different surface environments. The syntheses and treatment are briefly described here. **Sample 1.** ZnS nanoparticles coated in mercaptoethanol (SHCH₂CH₂OH) were synthesized by combining aqueous solutions of Na₂S and ZnCl₂ at pH 10.2 in the presence of mercaptoethanol (23). **Sample 2.** Na₂S in methanol was added dropwise to a solution of ZnCl₂ in anhydrous methanol with constant stirring. Washing with additional anhydrous methanol to remove NaCl results in a suspension of approximately 3 nm ZnS nanoparticles in pure methanol (9). **Sample 3.** DI water was added to ZnS nanoparticles in methanol (i.e. **sample 2**) to give a final water concentration of 10% v/v. The interaction of water with the nanoparticle surface drives a structural transformation within the nanoparticles without change of particle size (9). **Sample 4.** Uncoated ZnS nanoparticles in water were obtained by adding dropwise a solution of 4.8 g of Na₂S in 200 ml DI water to 2.7 g of ZnCl₂ in 300 ml DI water adjusted to pH 11 with NaOH. **Sample 5.** Pure synthetic bulk ZnS powder (greater than 100 nm grain size) was obtained by treating commercial sphalerite at 200 C in 1M NaOH in a hydrothermal bomb.

All nanoparticles from the above syntheses were determined by to be nanoscale and approximately in the cubic sphalerite (zinc blende) phase, from ultraviolet-visible (UV-vis) absorption spectroscopy and x-ray diffraction (XRD) measurements respectively. A more precise determination of particle size was

made with small-angle x-ray scattering (SAXS) measurements from diluted samples in the appropriate solvents (25)(26). The nanoparticle diameters obtained in this way were checked to be consistent with transmission electron microscopy (TEM), e.g. **Figure 1a**.

SAXS measurements on the nanoparticle samples were performed at beamline 5-ID-D at the APS (**samples 1 - 3**) or beamline 1-4 at the SSRL (**sample 4**). Two-dimensional scattering patterns were corrected for detector background and the solvent contribution and integrated using standard methods (24). ZnS nanoparticles synthesized without surface capping molecule (mercaptoethanol) were observed to aggregate. Thus, the SAXS curves were fitted by spherical particles with a Schultz distribution of diameters (see e.g. ref. (27)) in an aggregate that is described by Teixeira's expression for fractal aggregates (28). We checked that this expression gives accurate size determination in the presence of aggregation by comparing the results from **sample 4** in both dispersed and aggregated states. The aggregated sample was prepared by slow evaporation of water from the sample until a gel was formed. **Figure 1a & b** shows the SAXS data and fits for all samples; the best-fit results are summarized in **Table 1**.

Nanoparticle structure and disorder was determined using wide-angle x-ray scattering (WAXS) at beamline 11-ID-B at the APS with a photon energy of 93 keV and using a two-dimensional image plate detector (29). WAXS patterns recording the scattering intensity vs. diffraction vector magnitude, q , were acquired from ZnS nanoparticles as a suspension in the appropriate solvent (**samples 1 and 2**) or as a dried powder (**samples 3 – 5**). The magnitude of the diffraction vector $q = (4\pi/\lambda)\sin\theta$, where the x-ray wavelength, $\lambda = 0.10775 \text{ \AA}$ and 2θ is the scattering angle. The diffraction intensity was treated by subtracting the backgrounds from the sample cell and solvent (where applicable) and normalizing, using atomic form factors and Compton scattering factors obtained from the literature (30)(31). The smooth atomic scattering contribution to the intensity is removed to produce the structure factors for each sample, which possess all the structural information. The structure factors were multiplied by the q scattering axis and Fourier transformed to give the real-space pair distribution functions (PDF) (32).

Figure 2 shows the q -weighted structure factors and associated PDFs for each sample. Excess strain and disorder within spherical nanoparticles can be shown visually by comparing the PDF obtained for real nanoparticles with a PDF that is simulated for a powder of the bulk material but with the size of the real nanoparticles. This procedure is described below and in [ref.\(18\)](#). For comparison, the experimental PDF for bulk ZnS is included in Figure 2.

The surface chemistry of the samples was analyzed with Fourier transform infrared spectroscopy (FTIR). The samples were dried in a vacuum oven at 50 °C, and then degassed at $\sim 1 \times 10^{-6}$ Torr overnight at 150 °C. Samples that were degassed at room temperature or at 150 °C gave identical XRD patterns, and no additional surface species were created by the high temperature treatment. The clean samples were placed in a dry N₂ atmosphere and portions were mixed with anhydrous KBr and pressed into a pellet for FTIR. FTIR was performed with a Nicolet 8700 spectrometer (32 – 1024 scans at a resolution of 4 cm⁻¹) with continuous flow of dry N₂. A blank KBr pellet was used as a reference for the handling procedure, and showed no detectable water contamination during sample handling and data acquisition.

RESULTS AND DISCUSSION.

Data from SAXS and TEM (**Fig. 1**) and UV-vis absorption spectroscopy indicate that the ZnS nanoparticles in all four samples are of a similar size. As shown in **Table 1**, the mean nanoparticle radii vary between 14.3 – 17.1 Å.

All the diffraction peaks from **samples 1, 3, and 4** in **Fig. 2a** can be attributed to the cubic sphalerite phase of ZnS, with no evident trace of the hexagonal (wurtzite) phase. However, the low stacking fault energy in ZnS leads to the facile formation of polytype structures that can be difficult to detect with x-ray diffraction alone. Stacking faults have been observed in TEM images of CdS nanoparticles (23). We previously observed that ZnS nanoparticles synthesized in water (**sample 4**) frequently contained stacking faults but mercaptoethanol coated nanoparticles (**sample 1**) contained many fewer stacking

faults. (33). Phase analysis is challenging for **sample 2** due to the extreme peak broadening. However, the XRD data are consistent with a highly strained sphalerite structure. The XRD data indicate no detectable bulk oxides in any sample.

The diffraction data additionally show that the samples possess a considerable range of internal structural disorder. Diffraction measurements on nanoparticles are sensitive to both particle size and disorder, both of which cause diffraction peak broadening. As all samples contain nanoparticles of approximately the same size, the larger diffraction peak widths and lower PDF intensities can be attributed only to internal disorder. Provided the size is determined independently (e.g. by SAXS), there is a straightforward method of separating the two contributions to the PDF data. The PDF displays all characteristic interatomic distances in a material: the shortest bond-length produces the first peak. In nanoparticles, the maximum interatomic distance that can contribute to the PDF is limited by the particle diameter. Although interatomic scattering may occur between atoms in different nanoparticles, the nanoparticles are on average not aligned with the precision of atoms in a crystal and so interparticle scattering does not contribute to the PDF and can be neglected. The effect of small particle size is therefore to contribute an envelope function in real space that reduces the PDF peak intensity at greater interatomic distance. For spherical nanoparticles, the finite size envelope function can be calculated analytically and provides a method to account quantitatively for finite size in PDF measurements (18).

Figure 2c compares the PDF from **sample 4** with a PDF simulated by applying an envelope function to the experimental PDF of bulk cubic ZnS. Because the simulation uses the experimental data for the bulk sample, rather than using a completely theoretical simulation, important experimental parameters, such as the energy resolution of the x-rays, are automatically included. To indicate how errors in nanoparticle size determination may affect this comparison, the simulated PDF is drawn as a broad line that encompasses the results for a range of diameters (3 – 3.8 nm). **Figure 2c** shows that when the finite particle size is considered, even the most crystalline of the samples studied contains more disorder than

present in bulk ZnS, and most samples are considerably more disordered. There is evidently a relationship between surface ligand and interior structure, which we addressed further with FTIR spectroscopy.

Figure 3 compares the infrared spectra from **samples 1** and **3**; FTIR data for water binding are summarized for all samples in **Table 2**. All exhibit a broad absorption band in the region 3000 - 3500 cm^{-1} that is associated with $\nu(\text{OH})$ stretching vibrations of liquid water with disordered hydrogen bonds. However, the $\delta(\text{HOH})$ bending vibrations of molecular water appear at different positions, 1620 cm^{-1} for **sample 4**, and 1608 cm^{-1} for **sample 3**. In both cases, this vibration is shifted to lower wavenumbers with respect to pure liquid water (1638 cm^{-1}). The spectrum of **sample 4** exhibits a relatively sharp $\nu(\text{OH})$ stretching vibration at 3670 cm^{-1} that can be attributed to surface bound zinc hydroxyl groups (37)(38), that is not present in any other spectra. In addition, the group of peaks around 1000 cm^{-1} is indicative of sulfate groups (37). As there is no evidence of a distinct ZnO phase from any diffraction data, the FTIR data therefore indicate that the oxidized groups are confined to the nanoparticle surface. No other samples showed evidence of surface oxidation, indicating that it was not caused by the degassing procedure prior to FTIR analysis.

The shift of the $\delta(\text{HOH})$ vibration to lower wavenumbers relative to liquid water is indicative of molecular water that is bound to a surface. This trend has been observed for water bound to nanoparticles of diamond (34) and for water in clays (36). In our study, FTIR spectroscopy of synthetic bulk ZnS after the degassing procedure showed that this sample was not oxidized, and gave a $\delta(\text{HOH})$ vibration at 1638 cm^{-1} . This value is identical to that for pure liquid water, as reported previously for water on bulk ZnS (39). Hence, the binding of water to the surface of ZnS nanoparticles occurs at distinct sites from the surface of microscopic grains of cubic ZnS. The hexagonal and cubic phases of bulk ZnS possess different surface sites (39), but neither the WAXS nor FTIR data can be explained by assuming that the nanoparticles have the hexagonal structure. Modified surface sites are

commonly predicted for nanoparticles (40) and inferred from experimental studies (18). Consequently, nanoparticles likely exhibit reconstructed, strained, or highly faceted surfaces. Alternatively, the electronic properties (e.g. Lewis acid strength) of binding sites may be modified in small particles due to boundary effects or more pervasive structural perturbations.

From the FTIR data, we can derive descriptions of the surfaces of each nanoparticle type. The observation of SH groups in the spectrum from **sample 3** indicates that mercaptoethanol is bound electrostatically to surface zinc atoms, without deprotonation or formation of covalent thiol bond to surface sulfur atoms. Molecular water is bound electrostatically to all samples, but dissociated water forms metal-hydroxyl groups at the surface of **sample 4** only. The presence of sulfur oxides indicates partial oxidation of **sample 4**. As this is not associated with sample handling after synthesis, and separate oxide phases are not observed with x-ray diffraction, the partial oxidation is likely confined to the immediate surface.

We were not able to observe whether methanol has any significant surface bonding, but we anticipate weak surface interactions. Water binding stabilizes a more crystalline structure, similar to that stabilized by mercaptoethanol. Both these species are anticipated to bind electrostatically to surface zinc atoms, leaving sulfur atoms underbonded. The structure with water is slightly more crystalline than with mercaptoethanol, suggesting that steric hindrance of the larger mercaptoethanol molecules allows binding to fewer surface atoms. Both covalent binding of hydroxyl to zinc and the presence of oxidized sulfur atoms results in the most crystalline material of all. For II-VI semiconductor nanoparticles, electrostatic passivation of surface cations by negatively charged ligands has generally been employed (12)(42). Passivation of surface anions is much less well studied, see [ref \(43\)](#). We predict that capping nanoparticle surfaces in such a way that both surface anion and cations are fully bonded will produce the most crystalline nanoparticles.

CONCLUSIONS

We combined PDF analysis of nanoparticle structure with particle size analysis and FTIR to reveal that the nature of surface solvent or ligand interactions can effect the interior crystallinity of nanoparticles. The availability of particles with a range of crystallinity provides a model system in which it will be possible to determine how interior disorder affects important nanoparticle properties, such as mechanical stiffness and fluorescent quantum yield.

ACKNOWLEDGMENTS Small-angle x-ray scattering data were acquired at beamline 5-ID-D of the Advanced Photon Source (APS) with the support of Steve Weigand, and at beamline 1-4 at the Stanford Synchrotron Radiation Laboratory with the support of John Pople. Wide-angle x-ray scattering data were acquired at beamline 11-ID-B at the APS with the support of Yang Ren. TEM data were acquired at the National Center for Electron Microscopy with the support of Chegyu Song. We thank Michael Martin for access to the Nicolet FTIR spectrometer. Funding for this work was provided by a grant from the Department of Energy Chemical Sciences Program ER 15218 and the National Science Foundation NIRT program EAR0123967 and by the Director, Office of Science, of the U.S. Department of Energy under Contract No. DE-AC02-05CH11231.

REFERENCES

- (1) Alivisatos, A. P. *Science* **1996**, *271*, 933.
- (2) Murray, C. B.; Norris, D. J.; Bawendi, M. G. *J. Am. Chem Soc.* **1993**, *115*, 8706.
- (3) Ranade, M. R.; Navrotsky, A.; Zhang, H. Z.; Banfield, J. F.; Elder, S. H.; Zaban, A.; Borse, P. H.; Kulkarni, S. K.; Doran, G. S.; Whitfield, H. J. *Proc. Nat. Acad. Soc.* **2002**, *99 supp. 2*, 6476.
- (4) Zhang, H.; Banfield, J. F. *J. Mater. Chem.* **1998**, *8*, 2073.

- (5) Leung, K.; Whaley, K. B. *J. Chem. Phys.* **1999**, *110*, 11012.
- (6) Wang, L.-W.; Zunger, A. *Phys. Rev. B* **1996**, *53*, 9579.
- (7) Rabani, E. *J. Chem. Phys.* **2001**, *115*, 1493.
- (8) Puzder, A.; Williamson, A. J.; Reboredo, F. A.; Galli, G. *Phys. Rev. Lett.* **2003**, *91*, 157405.
- (9) Zhang, H.; Gilbert, B.; Huang, F.; Banfield, J. F. *Nature* **2003**, *424*, 1025.
- (10) Gilbert, B.; Huang, F.; Zhang, H.; Ren, Y.; Haskel, D.; Lang, J. C.; Srajer, G.; Jürgenssen, A.; Waychunas, G. A.; Banfield, J. F. *J. Chem. Phys.* **2004**, *120*, 11785.
- (11) Stoneham, A. M. *Theory of Defects in Solids*. Clarendon Press, Oxford (1985).
- (12) Hellmann, R.; Euteneuer, A.; Hense, S.G.; Feldmann, J.; Thomas, P.; Göbel, E.O.; Yakovlev, D.R.; Waag, A.; Landwehr, G. *Phys. Rev. B* **1995**, *51*, 18053.
- (13) Rockenberger, J.; Tröger, L.; Rogach, A. L.; Tischer, M.; Grundmann, M.; Eychmüller, A.; Weller, H. *J. Chem. Phys.* **1998**, *108*, 7807.
- (14) Marcus, M. A.; Flood, W.; Steigerwald, M.; Brus L.; Bawendi. M. G. *J. Phys. Chem.* **1991**, *95*, 1572.
- (15) Carter, A. C.; Bouldin, C. E.; Kemner, K. M.; Bell, M. I.; Woicik, J. C.; Majetich, S. A. *Phys. Rev. B* **1997**, *55*, 13822.
- (16) Bawendi, M. G.; Kortan, A. R.; Steigerwald, M. L.; Brus, L. E. *J. Chem. Phys.* **1989**, *91*, 7282.
- (17) Vogel, W.; Urban, J.; Kundu, M.; Kulkarni, S. K. *Langmuir* **1997**, *13*, 827.
- (18) Gilbert, B.; Huang, F.; Zhang, H.; Waychunas, G. A.; Banfield, J. F. *Science* **2004**, *305*, 651.
- (19) Son, D. H.; Hughes, S. M.; Yin, Y.; Alivisatos, A. P. *Science* **2004**, *306*, 1009

- (20) Huang, F.; Gilbert, B.; Zhang, H.; Banfield, J. F. *Phys. Rev. Lett.* **2004**, *92*, 155501
- (21) Rajh, T.; Chen, L. X.; Lukas, K.; Liu, T.; Thurnauer, M. C.; Tiede, D. M.; *J. Phys. Chem. B* **2002**, *106*, 10543.
- (22) Wuister, S. F.; Donega, C. M.; Meijerink, A. *J. Am. Chem. Soc.* **2004**, *126*, 10397.
- (23) Vogel, W.; Borse, P. H.; Deshmukh, N.; Kulkarni, S. K. *Langmuir* **2000**, *16*, 2032
- (24) Hammerly, A. P.; Fit2D. Internal Report ESRF98HA01T. European Synchrotron Radiation Facility, Grenoble, France.
- (25) Hamad, S.; Cristol, S.; Catlow, C. R. A.; *J. Phys. Chem.* **2002**, *106*, 11002.
- (26) Kotlarchyk, M.; Chen, S.-H. *J. Chem. Phys.* **1983**, *79*, 2461.
- (27) Gazzillo, D.; Giacometti, A. *J. Chem. Phys.* **2000**, *113*, 9837.
- (28) Teixeira, J. *J. App. Cryst.* **1988**, *21*, 781
- (29) Chupas, P. J.; Qiu, X.; Hanson, J. C.; Lee, P. L.; Grey, C. P.; Billinge, S. J. L. *J. App. Cryst.* **2003**, *36*, 1342.
- (30) Thijssen, B. J.; *J. Appl. Cryst.* **1984**, *17*, 61.
- (31) Egami, T. (1998). *Local Structure from Diffraction*, edited by S. J. L. Billinge & M. F. Thorpe, p. 1. New York: Plenum.
- (32) Toby, B. H.; Egami, T. *Acta Cryst.* **1992**, *A48*, 336.
- (33) Huang, F.; Zhang, H.; Banfield, J. F. *J. Phys. Chem. B* **2003**, *107*, 10470.
- (34) Guinier, A. (1963) *X-ray diffraction in crystals, imperfect crystals and amorphous bodies*. W.H. Freeman & Co., San Francisco.

- (35) Ji, S.; Jiang, T.; Xu, K.; Li, S. *Applied Surface Science* **1998**, *133*, 231.
- (36) Johnston, C. T.; Sposito, G.; Erickson, C. *Clays and Clay Minerals* **1992**, *40*, 722.
- (37) Little, L. H. *Infrared Spectra of Adsorbed Surface Species*; Academic Press, New York, 1966.
- (38) Koretsky, C. M.; Sverjensky, D. A.; Salisbury, J. W.; D'Aria, D. M.; *Geochim. Cosmochim. Acta* **1997**, *61*, 2193.
- (39) Hertl, W.; *Langmuir* **1988**, *4*, 594.
- (40) Puzder, A.; Williamson, A.J.; Gygi, F.; Galli, G. *Phys. Rev. Lett.* **2004**, *92*, 217401.
- (41) FTIR analysis of ZnS nanoparticles in pure methanol gave quantitatively similar results to nanoparticles in methanol following the addition of water. Trace water in solution was evidently concentrated during drying.
- (42) Vossmeier, T., Katsikas, L., Gienig, M., Popovic, I. G., Diesner, K., Chemseddine, A., Eychmiiller, A. & Weller, H. *J. Phys. Chem.* **1994**, *98*, 7663-7673.
- (43) Ni, T., Nagesha, D. K., Robles, J., Materer, N. F. Müssig, S. & Kotov, N. A. *J. Am. Chem. Soc.* **2002**, *124*, 3980-3992.

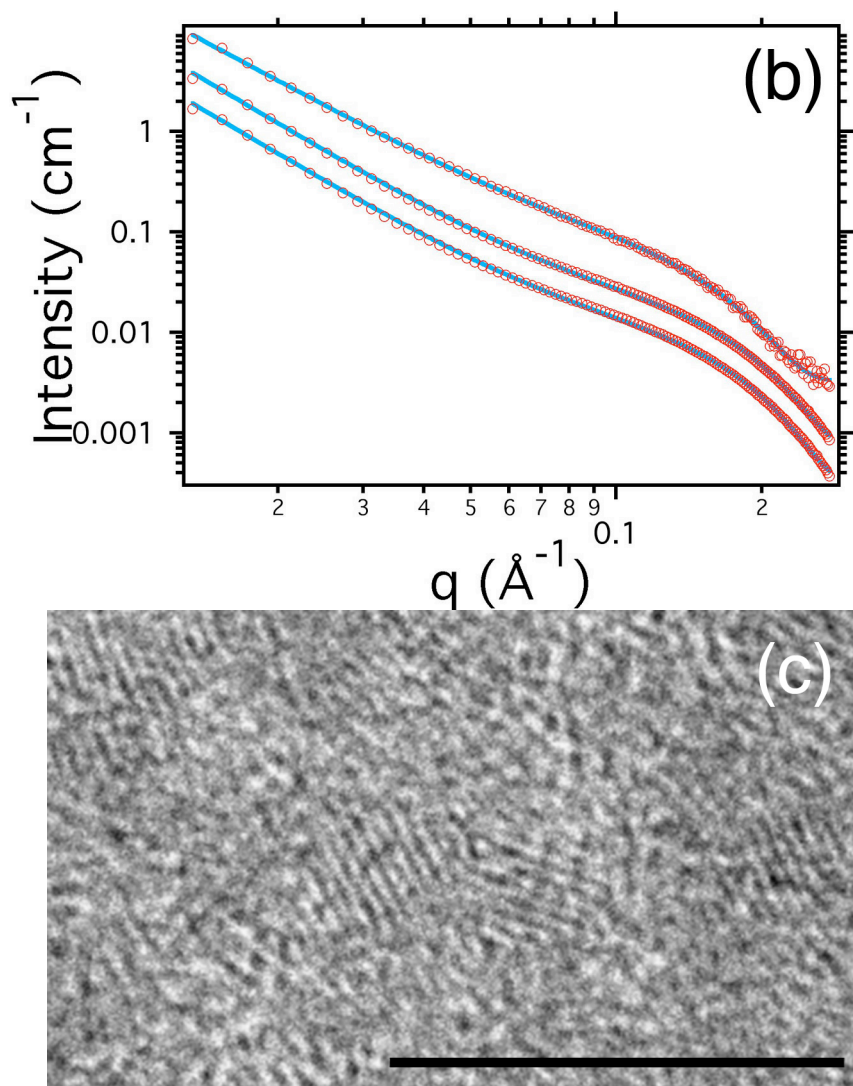


Figure 1. Small-angle x-ray scattering (SAXS) and transmission electron microscopy (TEM) determination of nanoparticle size. **(a)** SAXS patterns for mercaptoethanol-coated ZnS nanoparticles in a dilute dispersion (lower curve) or aggregated in a gel (**sample 1**). **(b)** SAXS patterns for ZnS nanoparticle aggregates in different solvents: in water at pH 10 (**sample 4**), in methanol (**sample 2**), and in 10% water in methanol (**sample 3**). Curves for samples 2 and 3 are offset for clarity. Circles = data, lines = fit. **(c)** TEM image of individual mercaptoethanol-coated ZnS nanoparticles (**sample 4**). At least three individual nanoparticles can be identified by lattice fringes. Scale bar = 10 nm.

Sample number	1	1, agg	2	3	4
Surface coating	SHEtOH	SHEtOH	methanol	water	oxidized
Mean radius (Å)	17.4	17.6	14.3	14.5	16.1
Radius spread (Å)	0.6	0.8	1.0	1.0	0.6
Fractal dimension	n/a	2.2	2.6	2.6	2.1

Table 1. Best-fit parameters following fits to SAXS data in Fig. 1.

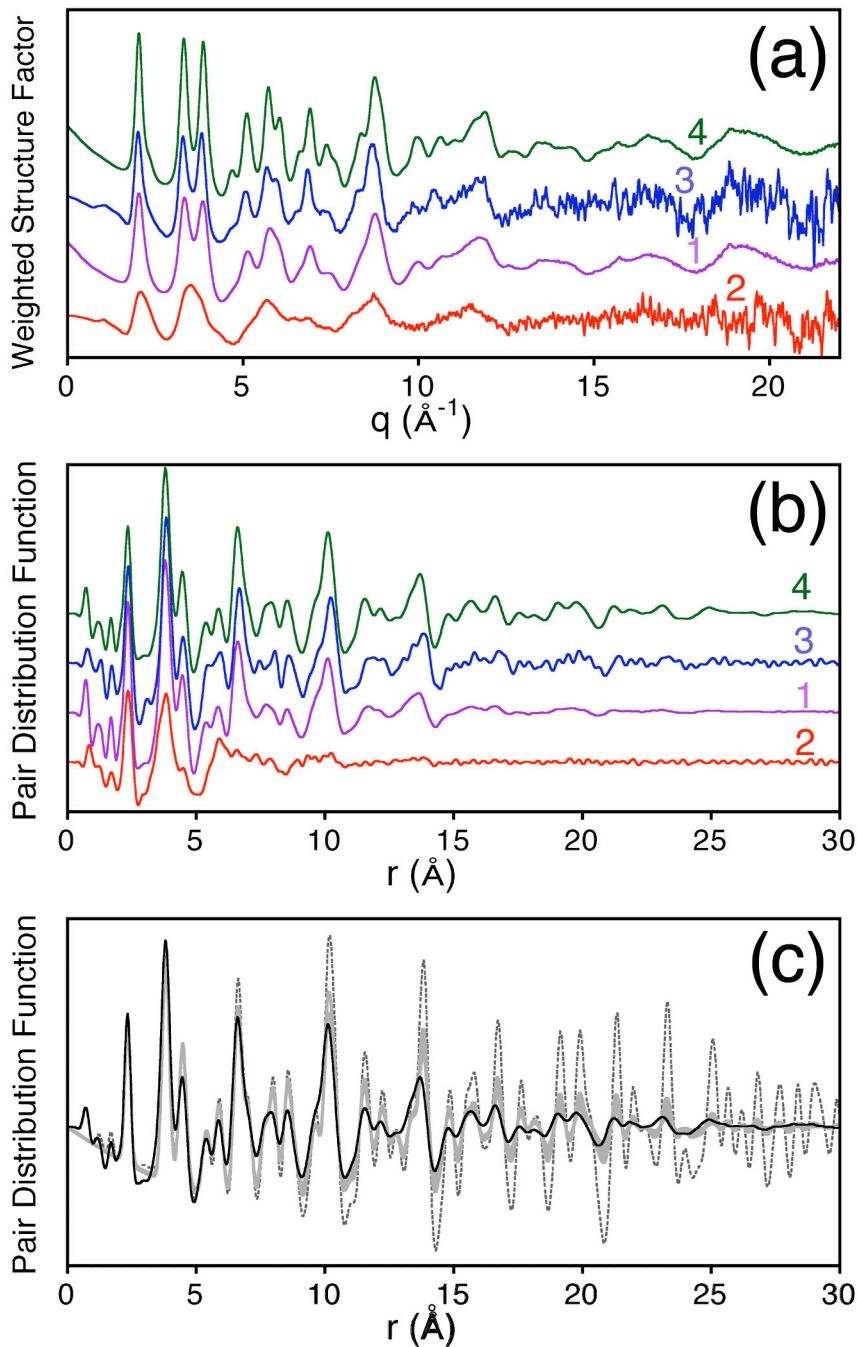


Figure 2. Wide-angle x-ray scattering (WAXS) analysis of ZnS nanoparticles. **(a)** The q -weighted structure factors for Samples 1-4, plotted with vertical offsets, ordered by increasing crystallinity. The diffraction vector, q , is defined in the text. **(b)** The corresponding real-space pair distribution functions (PDF). **(c)** Comparison of the experimental PDF of bulk cubic ZnS (dashed line), the simulated PDF of a 3.3–3.5 nm diameter nanoparticle with the bulk cubic ZnS structure (thick gray line), and the

experimental PDF of 3.4nm nanoparticles (thin black line, Sample 4). Data from Samples 2 and 3 were acquired in solution, resulting in poorer signal to noise than other samples measured as powders.

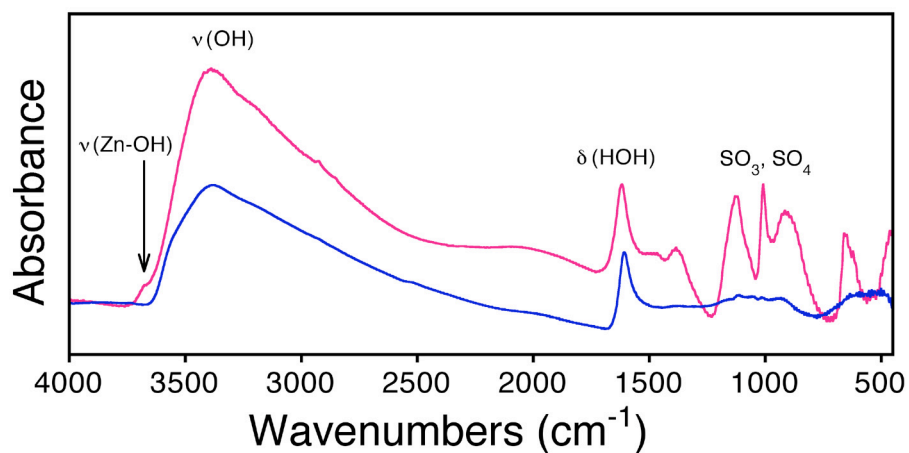


Figure 3. Fourier transform infrared spectra from ZnS nanoparticles synthesized in water at pH 11 (top, **sample 4**), and from nanoparticles synthesized in methanol, 24 hours after the addition of water (bottom, **sample 2**).

Sample number	nanoparticles				bulk
	1	2	3	4	5
Surface coating	SHEtOH	methanol	water	oxidized	water
$\nu(\text{Zn-OH}) / \text{cm}^{-1}$	-	-	-	3670	-
$\delta(\text{HOH}) / \text{cm}^{-1}$	1615	-	1608	1620	1638

Table 2. Positions of infrared absorption peaks associated with surface hydroxyl groups and bound molecular water on ZnS nanoparticles and synthetic bulk cubic ZnS.

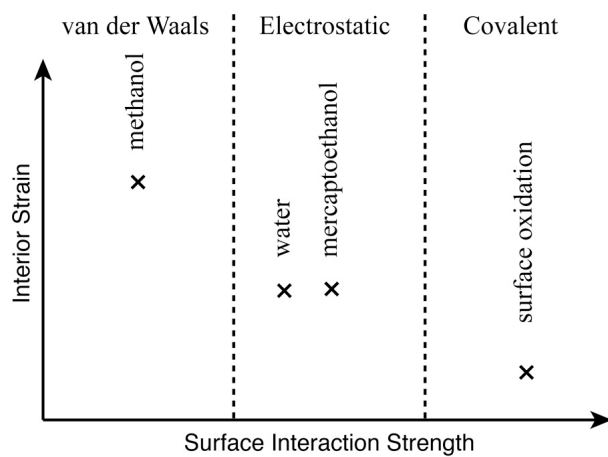


Figure 4. Scheme indicating the variation of strain within 3 nm ZnS nanoparticles for different surface interactions.